Solar Energy 173 (2018) 665–674

Contents lists available at ScienceDirect

Solar Energy

journal homepage: www.elsevier.com/locate/solener

Plasmon heating of one-dimensional gold nanoparticle chains

Xin Yan[a], Guohua Liu[a,*], Jinliang Xu[a,b,*], Shuai Wang[b]

[a] Beijing Key Laboratory of Multiphase Flow and Heat Transfer for Low Grade Energy Utilization, North China Electric Power University, Beijing 102206, PR China
[b] Key Laboratory of Condition Monitoring and Control for Power Plant Equipment of Ministry of Education, North China Electric Power University, Beijing 102206, PR China

ARTICLE INFO

Keywords:
Solar energy
Plasmon heating
Nanoparticle chain
Boundary effect

ABSTRACT

Metallic nanoparticle chains exhibit strong plasmon coupling in periodic arrays that provides numerous opportunities for manipulating heating at nanoscale. The energy transport in a chain is sensitive to the interparticle plasmon coupling. A better understanding of optical and heating properties of the chain would provide useful guidance for future design of the novel devices. In this work, we use the organization of gold nanoparticles as linear assemblies and perform a detailed analysis of the heating features as a function of the number of particle, interparticle spacing and particle size in the chains using General Mie Theory. The results show that the heat generation of particle presents an exponential decay with increasing of the interparticle spacing. As the number of particle increases, the particle spacing increases and radius decreases, the boundary effect is gradually diminished to the center particle. When the particle spacing is 1 nm, the number of particle is seven and the radius is 10 nm, the heat production of center particle is 1.65 times than that of a single particle. The large particle size effectively increases the cross-section of absorption as well as the range of electromagnetic radiation, and thus more light energy can be absorbed and converted into heat as the radius increases. This study provides an original understanding on the plasmon heating behavior of one-dimensional nanoparticle chains and may be generalized to other types of aggregates formed by large numbers of interacting particles.

1. Introduction

Metallic nanoparticle assemblies separated by nanometric gaps exhibit strong plasmon coupling that support increasing application in renewable energy, electronics, sensing and communications (Herrmann et al., 2014; Lal et al., 2007; Nie et al., 2010; Scanlon et al., 2018; Wang et al., 2017). Various strategies such as lithographic techniques (Hicks et al., 2005), DNA-based method (Kuzyk et al., 2012; Tan et al., 2011), molecularly linked systems (Lin et al., 2005; Teulle et al., 2015), electrostatic interactions (Zhang and Wang, 2008) have been suggested for synthesis of the nanoassemblies. A series of well-defined nanoassemblies from nanoparticle chains to aggregates of few particles have been demonstrated (Esteban et al., 2012b; Fan et al., 2010; Manoharan et al., 2003; Wang et al., 2012). Interparticle coupling effect in these assemblies results in unique, coherent optical properties since the distance between the particles can be tuned for near field coupling of their surface plasmon resonances (Citrin, 2004; Ghosh and Pal, 2007; Halas et al., 2011; Hentschel et al., 2010). The electromagnetic couplings induce photonic effects that can interact with plasmon excitation in individual particle to alter the plasmon lineshape.

The shift of plasmon coupling band strongly depends on the extent of interaction between nanoparticles (Barrow et al., 2014; Jung et al., 2015; Ross et al., 2016; Zou and Schatz, 2006). The large spacing above hundred nanometer lead to distinct retardation and radiative contributions to the dipolar interactions between particles that produces blue-shifted plasmon lineshapes (Downing et al., 2018; Haynes et al., 2003). While if the interparticle gaps are small compared to the plasmon wavelength, this coupling would give rise to red-shifted plasmon bands in extinction spectra (Jain et al., 2007). This redshift can be explained by hybridization of the dipolar plasmon modes (Nordlander et al., 2004). As the interparticle gap at subnanometer range, the influence of surrounding charge distribution becomes significant. These nonlocal effects lead to a smaller redshifting plasmon bands compared to the classical local description (Esteban et al., 2012a; Mortensen et al., 2014). A further decrease in the interparticle spacing promotes electron tunneling across the gaps. The tunneling current neutralizes the capacitive charges across the junction, causing blue-shift plasmon bands (Tserkezis et al., 2014; Zhu and Crozier, 2014; Zuloaga et al., 2009). The intensity of local electric field also decreases in this quantum regime because of the charge screening at gap by electron transfer.

* Corresponding authors at: Beijing Key Laboratory of Multiphase Flow and Heat Transfer for Low Grade Energy Utilization, North China Electric Power University, Beijing 102206, PR China (J. Xu).
E-mail addresses: liuguohua@ncepu.edu.cn (G. Liu), xjl@ncepu.edu.cn (J. Xu).

https://doi.org/10.1016/j.solener.2018.08.003
Received 28 May 2018; Received in revised form 4 July 2018; Accepted 1 August 2018

Nomenclature

$\boldsymbol{k}$	wave vector, $k = 2\pi/\lambda$
$\boldsymbol{E}$	electric field intensity
$\boldsymbol{M}$, $\boldsymbol{N}$	vector function
$Y_{lm}(\theta, \phi)$	un-normalized generalized Legendre functions
l, p	indicate $l(p) = 0,1,2,3,\ldots$
m, q	indicate $m(q) = -l(p), -l(p)+1\ldots, 0\ldots, l(p)-1, l(p)$
$z(kr)$	expression of spherical Bessel function
$j(kr)$	first kind spheric Bessel function
$y(kr)$	the second kind spheric Bessel function
$h^{(1)}(kr)$	the first kind spheric Hankel functions
$h^{(2)}(kr)$	the second kind spheric Hankel functions
(r, θ, ϕ)	spherical coordinate system
(i_r, i_θ, i_ϕ)	standard unit vectors associated with the coordinates (r, θ, ϕ)
f, g	expansion coefficient for incident field
a, b	expansion coefficient for internal field
c, d	expansion coefficient for scattered field
r_p	nanoparticle radius
n	number of nanoparticles
n_1	particle complex refractive index
n_2	ambient medium refractive index
A, B	coordinate conversion factor
C, D	Mie scattering coefficient
$J_{l+1/2}(\chi)$	first kind Semi-integer Bessel function
L	nanoparticle center distance
D_p	nanoparticle diameter
R_{ij}	distance between two local coordinate system origin
$\boldsymbol{S}$	poynting vector
P	power
I	incident light irradiance
C_{abs}	absorption coefficient
$\boldsymbol{p}$	polarization intensity of the nanoparticle

Greek symbols

ε_1	dielectric constant of particle
ε_2	dielectric constant of surrounding medium
ε_0	permittivity of vacuum
λ	wavelength
δ	nanoparticle spacing
α	angle between the line of the origins of two coordinates and z axis
β	angle between the line of the origins of two coordinates and x axis
ψ_l	first kind Ricatti-Bessel functions
χ	dimensionless nanoparticle size factor
ρ	relative refractive index

Subscripts

l	indicate $l(p) = 0,1,2,3,\ldots$
m	indicate $m(q) = -l(p), -l(p)+1\ldots, 0\ldots, l(p)-1, l(p)$
inc	incident light/field
in	nanoparticle inside
sca	scattering
out	nanoparticle outside
surf	nanoparticle surface
0	initial incident light
i, j	the $i(j)$th nanoparticle
ext	extinction
abs	absorption
Re	real part
Im	imaginary part
p	nanoparticle

Interparticle plasmon coupling allows fine control over the optical and heating properties for different purposes (Baffou et al., 2010; Chen et al., 2018; Lee et al., 2012; Sanchot et al., 2012; Tian et al., 2015). A semianalytical model has been derived to investigate the light scattering properties of gold nanoparticle chains (Barrow et al., 2011; Thomas and Swathi, 2016). The chain plasmon mode was found to depend on the interparticle coupling strength and the dielectric constant of the background medium. Nanoparticle chains can serve as a plasmon waveguide to overcome the diffraction limit of the optical image (Lal et al., 2007; Maier et al., 2003). Imaging of proteins labeled with gold nanoparticles were realized by using an optical method based on photo-thermal interference contrast (Cognet et al., 2003). Controlled drug release was achieved by a capsule containing Au nanoparticles excited with intense light (Skirtach et al., 2005). Nanoscale heat generation of gold nanoparticles has been characterized during a melting process in ice matrix (Richardson et al., 2006). It was found that the heating process has a mesoscopic character and strongly depended on the geometry of nanoparticle ensemble (Govorov et al., 2006). Recently, the reversible plasmonic assemblies become a hot research area that offering the new opportunity to tune the optical, mechanical, catalytic and heating properties of materials with promising applications in fields ranging from biosensors to nanorobotics and energy (Ding et al., 2016; Montelongo et al., 2017; Qian and Ginger, 2017; Scanlon et al., 2018).

In this context, understanding of the plasmon heating and their coupling is critical important for the innovation of these fields. As a simple model, nanoparticle chains is an interesting system for understanding the interactions of light with matter. In such structure, light is not only absorbed by a single particle, but excites collective plasmon modes that exist over the entire chain. Herein, gold nanoparticle chains are selected as the plasmon-coupling model. The General Mie Theory (GMT) method is introduced to study the factors affecting the plasmon heating. The role of the number of particle, particle radius and interparticle spacing in the chain are systematically examined to understand the interparticle coupling as well as energy propagation along the chains. This study could be useful to guide design of photoresponsive plasmon devices for heat-sensitive applications.

2. Methods

The calculation model is finite one-dimensional plasmonic chains (Fig. 1). The spherical gold nanoparticles are arranged along the x direction. r represents the particle radius and δ is the interparticle spacing. The relative dielectric constant of Au adopts the experimental data from reference (Johnson and Christy, 1972), and that of the water (surrounding environment) is ~1.76. The origin of global coordinate system locates at the center of first particle. The incident light propagate on the wave vector $\boldsymbol{k}$ along the positive direction of z-axis. The radiation intensity of light is one sun (~1 kW/m^2). The solar-spectral data comes from ASTM in 2012 (G173, 2007). Since sunlight is non-polarized light, it can be decomposed into two linearly polarized lights at same intensity with vibration perpendicular to each other. The two linearly polarized lights are independent of each other. For example, the wave vector $\boldsymbol{k}$ in z direction can be decomposed into a linearly polarized light in x direction and another linearly polarized light in y direction (see the inset in Fig. 1b). Therefore, the heat production of particle also can be divided into two parts. One is induced by vibration of light in x direction and the other resulted from light vibration along y direction.

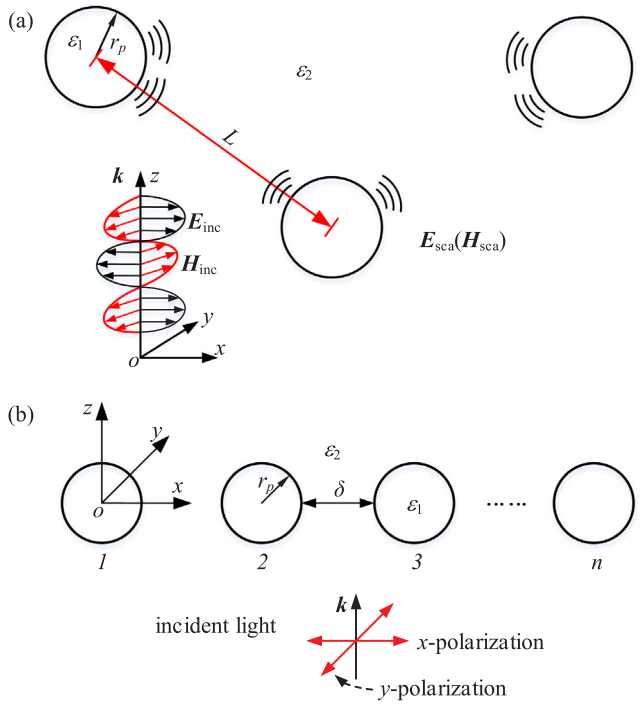

Fig. 1. (a) Diagram of scattering field interaction and (b) calculation model.

2.1. General Mie Theory

GMT is established upon the superposition principle of electric field (Mie, 1908). The electric field in space is the result of superposition of multiple particles scattering field $\boldsymbol{E}_s(i)$ and incident field $\boldsymbol{E}_{inc}$. According to *Electromagnetic Theory* (Jackson, 2001) the linear independent vector wave functions $\boldsymbol{M}_{lm}$ and $\boldsymbol{N}_{lm}$ based on spherical coordinates are described here to simplify the mathematic description of the electric fields.

$$\boldsymbol{M}_{lm} = imz_l(kr)\frac{Y_{lm}(\theta,\varphi)}{\sin(\theta)}\boldsymbol{i}_\theta - z_l(kr)\frac{\partial Y_{lm}(\theta,\varphi)}{\partial\theta}\boldsymbol{i}_\varphi \tag{1}$$

$$\boldsymbol{N}_{lm} = l(l+1)\frac{z_l(kr)}{kr}Y_{lm}(\theta,\varphi)\boldsymbol{i}_r + \frac{[krz_l(kr)]'}{kr}\frac{\partial Y_{lm}(\theta,\varphi)}{\partial\theta}\boldsymbol{i}_\theta + im\frac{[krz_l(kr)]'}{kr}\frac{Y_{lm}(\theta,\varphi)}{\sin(\theta)}\boldsymbol{i}_\varphi \tag{2}$$

where $\boldsymbol{i}_r$, $\boldsymbol{i}_\theta$, and $\boldsymbol{i}_\varphi$ are unit vectors associated with the coordinates r, θ, and φ, respectively, $z_l(kr)$ is the Bessel function of spherical coordinate system, which can be j_l, y_l, $h_l^{(1)}$ and $h_l^{(2)}$. $Y_{lm}(\theta,\varphi)$ is the un-normalized generalized Legendre functions. $\boldsymbol{k}$ is the wavenumber in the considered medium. The sign of ' ' represents derivation.

The electric field $\boldsymbol{E}$ is expressed as

$$\boldsymbol{E} = \sum_{lm}(a_{lm}\boldsymbol{M}_{lm}^{(n)} + b_{lm}\boldsymbol{N}_{lm}^{(n)}) \tag{3}$$

$\boldsymbol{M}_{lm}^{(n)}$ and $\boldsymbol{N}_{lm}^{(n)}$, $n = 1, 2, 3$, or 4, the$z_l(kr)$ represent the first kind spheric Bessel function $j_l(kr)$ when $n = 1$. It is the second kind spheric Bessel function $y_l(kr)$ when $n = 2$, or the spheric Hankel functions of the first and second kind $h_l^{(1)}(kr)$ and $h_l^{(2)}(kr)$, respectively. The incident electromagnetic field is described as

$$\boldsymbol{E}_{inc} = E_0\sum_{lm}(f_{lm}\boldsymbol{M}_{lm}^{(1)} + g_{lm}\boldsymbol{N}_{lm}^{(1)}) \tag{4}$$

f_{lm} and g_{lm} are determined by the incident light direction and the polarization direction of electric field. In this work, light is propagated in negative z direction and the polarization direction of electric field is along x axis. So the coefficient f_{lm} and g_{lm} can be treated as

$$f_{l1}(i) = -\frac{1}{2}i^{l+1}\frac{2l+1}{l(l+1)}e^{ik_2z_i}, \quad f_{l,-1}(i) = -\frac{1}{2}i^{l+1}(2l+1)e^{ik_2z_i} \tag{5}$$

$$g_{l1}(i) = f_{l1}(i), \quad g_{l1}(i) = f_{l1}(i) \tag{6}$$

$$g_{lm}(i) = g_{lm}(i) = 0, \quad |m| \neq 1 \tag{7}$$

In which, z_i represents the position of ith particle in global coordinate system. Similarly, electric field in particles is rewritten as

$$\boldsymbol{E}_{in} = E_0\sum_{lm}(a_{lm}\boldsymbol{M}_{lm}^{(1)} + b_{lm}\boldsymbol{N}_{lm}^{(1)}) \tag{8}$$

If $r < r_p$, $z_l(kr)$ in $\boldsymbol{M}_{lm}$ and $\boldsymbol{N}_{lm}$ is the first kind spheric Bessel function $j_l(kr)$ for limited solutions of the functions in particle centre. When $r > r_p$, for functions to be regular at infinity region, $z_l(kr)$ in $\boldsymbol{M}_{lm}$ and $\boldsymbol{N}_{lm}$ is the first kind spheric Hankel functions $h_l^{(1)}(kr)$.

$$\boldsymbol{E}_{sca} = E_0\sum_{lm}(c_{lm}\boldsymbol{M}_{lm}^{(3)} + d_{lm}\boldsymbol{N}_{lm}^{(3)}) \tag{9}$$

According to the superposition principle, the electric field in space can be represented by addition of the scattered particle field and incident field

$$\boldsymbol{E}_{out}(i) = \boldsymbol{E}_{sca}(i) + \sum_{j\neq i}^{n}\boldsymbol{E}_{sca}(j) + \boldsymbol{E}_{inc}(i) \tag{10}$$

where $\boldsymbol{E}_{out}(i)$ is electric field around the i-th particle, $\boldsymbol{E}_{sca}(i)$ the contribution of i-th particle's scattered field, $\boldsymbol{E}_{sca}(j)$ the contribution of j-th particle's scattered field to the electric field around the i-th particle, $\boldsymbol{E}_{inc}(i)$ the contribution of incident field to the electric field around the i-th particle. The boundary conditions of electric field at medium and particle interface needs to be continuous, and getting

$$[\boldsymbol{E}_s(i) + \sum_{j\neq i}^{n}\boldsymbol{E}_{sca}(j) + \boldsymbol{E}_{inc}(i) - \boldsymbol{E}_{in}(i)]\times\boldsymbol{r}|_{r=r_p} = 0 \tag{11}$$

The subscripts i and j denote the origin of reference coordinate system at the centre of i-th or j-th particle respectively. There are two coordinates systems in Eq. (11). For simplification, the coordinate system defined at the centre of j-th must be convert into the coordinate system based on i-th particle. Since the system formed by M_{lm} and N_{lm} is orthogonal and complete for transverse waves, by using a projection technique one has (Gérardy and Ausloos, 1982)

$$N_{pq}^{(3)}(j) = \sum_{l=0}^{\infty}\sum_{m=-l}^{l}B_{pqlm}(j,i)M_{lm}^{(1)}(i) + A_{pqlm}(j,i)N_{lm}^{(1)}(i) \tag{12}$$

$$M_{pq}^{(3)}(j) = \sum_{l=0}^{\infty}\sum_{m=-l}^{l}B_{pqlm}(j,i)M_{lm}^{(1)}(i) + A_{pqlm}(j,i)M_{lm}^{(1)}(i) \tag{13}$$

$A_{pqlm}(j,i)$ and $B_{pqlm}(j,i)$ will be stated later. Here, we combine the equations of (10), (12) and (13), and then obtain that

$$c_{lm}(i) = C_l(i)\left\{\sum_{j\neq i}^{n}\sum_{pq}[c_{pq}(j)A_{pqlm}(j,i) + d_{pq}(j)B_{pqlm}(j,i)] + f_{lm}(i)\right\} \tag{14}$$

$$d_{lm}(i) = D_l(i)\left\{\sum_{j\neq i}^{n}\sum_{qp}[d_{pq}(j)A_{pqlm}(j,i) + c_{pq}(j)B_{pqlm}(j,i)] + g_{lm}(i)\right\} \tag{15}$$

$C_l(i)$ and $D_l(i)$ reflect the response of particle scattering field to external incident field. They are the same as the Mie scattering coefficient $C_l(i)$ and $D_l(i)$ of single particle, which reflects the relationship between particle scattering field and external incident field. The coefficients are thus determined by the geometrical parameters and physical parameters of particle. Eqs. (14) and (15) are the iterative formulas to calculate the coefficients. The results of previous step of the same particle are compared with the current results. If error satisfies the

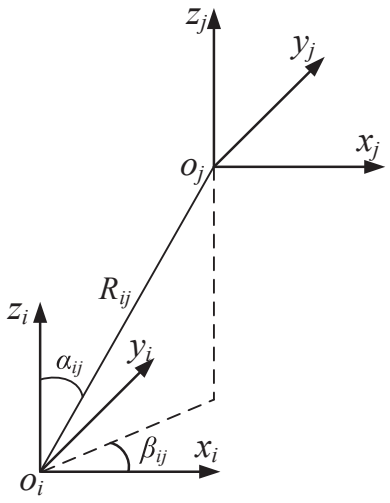

Fig. 2. The original coordinate system.

convergent requirement, the $c_{lm}(i)$ and $d_{lm}(i)$ are the final coefficients, else the current results are substituted into the equations to get new coefficients until the result is converged.

2.2. Transformation of coordinate system (Addition Theorem)

In normal condition, rectangular coordinate axes are located at the centre of particle *i* and *j* respectively, and the coordinate axes parallel to each other (Fig. 2). The distance between the origins of two frames is R_{ij}. The angle between the line of the origins of two coordinates and x_i axis is β_{ij}. The angle between the line of the origins and z_i axis is α_{ij}. $A_{pqlm}(i, j)$ and $B_{pqlm}(i, j)$ are given by the spherical harmonic function addition theorem as (Cruzan, 1962; STEIN, 1961)

$$A_{pqlm}(R_{ij}, \alpha_{ij}, \beta_{ij}) = (-1)^m \mathrm{i}^{l-p} \frac{2l+1}{2l(l+1)} \sum_n \mathrm{i}^n [p(p+1) + l(l+1) - n(n+1)] \times a(p, q: l, m: n) \times h_n^{(1)}(R_{ij}) P_n^{p-m}(\cos\alpha_{ij}) e^{\mathrm{i}(p-m)\beta_{ij}} \quad (16)$$

$$B_{pqlm}(R_{ij}, \alpha_{ij}, \beta_{ij}) = (-1)^{m+1} \mathrm{i}^{l-p} \frac{2l+1}{2l(l+1)} \sum_n \mathrm{i}^{n+1} \frac{2n+3}{2n+1} a(p, q: l, m: n) \times \{(l-m)(l+m+1) a(p, q: l, -m-1: n) + 2m(n-q+m+1) a(p, q: l, -m: n) - (n-q+m+1)(n-q+m) a(p, q: l, -m+1: n) \times h_{n+1}^{(1)}(R_{ij}) P_{n+1}^{p-m}(\cos\alpha_{ij}) e^{\mathrm{i}(p-m)\beta_{ij}} \quad (17)$$

where $a(p, q: l, m: o)$ is Gaunt coefficient (Cruzan, 1962).

2.3. Heat generation

Heat generation of particles is calculated based on Poynting vector $\boldsymbol{S} = \boldsymbol{E} \times \boldsymbol{H}$, and energy conservation law. For the scattering field of particle *i*, the Poynting vector is calculated as (Mackowski, 1991)

$$P_{ext}(i) = \frac{4\pi I}{k^2} \mathrm{Re} \sum_{lm} \frac{l(l+1)}{2l+1} \frac{(l+m)!}{(l-m)!} (f_{lm}^*(i) c_{lm}(i) + g_{lm}^*(i) d_{lm}(i)) \quad (18)$$

$$P_{sca}(i) = \frac{4\pi I}{k^2} \mathrm{Re} \sum_{lm} \frac{l(l+1)}{2l+1} \frac{(l+m)!}{(l-m)!} \{c_{lm}^*(i)[f_{lm}(i) + c_{lm}(i)(1-C_l)] + d_{lm}^*(i)[g_{lm}(i) + d_{lm}(i)(1-D_l)]\} \quad (19)$$

$$P_{abs}(i) = \frac{4\pi I}{|\rho_i|^2 k^2} \mathrm{Re} \sum_{lm} \mathrm{i} \frac{l(l+1)}{2l+1} \frac{(l+m)!}{(l-m)!} \psi_l'(\rho_i\chi_i) \psi_l^*(\rho_i\chi_i) (\rho_i^* |b_{lm}(i)|^2 + \rho_i |a_{lm}(i)|^2) \quad (20)$$

where the sign of '*' represents conjugate. The relationship between the internal field coefficient and the external scattering coefficient is as follows:

$$a_{lm}(i) = \frac{\mathrm{i}m_i}{\psi_l(m_i\chi_i)\psi_l'(\chi_i) - m_i\psi_l(\chi_i)\psi_l'(m_i\chi_i)} c_{lm}(i) \quad (21)$$

$$b_{lm}(i) = \frac{\mathrm{i}m_i}{m_i\psi_l'(\chi_i)\psi_l(m_i\chi_i) - \psi_l(\chi_i)\psi_l'(m_i\chi_i)} d_{lm}(i) \quad (22)$$

Here, $P_{abs}(i)$ is the energy absorbed by the particle *i*. ψ_l is first kind Ricatti-Bessel function, $\psi_l(x) = \sqrt{\frac{\pi x}{2}} J_{l+\frac{1}{2}}(\chi)$. ξ_l is first kind Ricatti-Hankel function, $\xi_l(\chi) = \sqrt{\frac{\pi\chi}{2}} h_{l+\frac{1}{2}}^{(1)}(\chi)$. ρ is relative refractive index, $\rho = \frac{n_1}{n_2}$. χ is dimensionless particle size parameter, $\chi = n_2 \frac{2\pi r_p}{\lambda}$.

2.4. Simulation procedure and validation

The calculation procedure is based on MATLAB programming. Fig. 3 shows the flow chart of simulation. Firstly, we determine the number of particle, particle radius *r* and interparticle spacing δ. The initial coefficient $c_{lm}(i)$ and $d_{lm}(i)$ is then given by single particle Mie scatter theory. Following that, we calculate the new scattering field coefficient from the first particle, then that of the second particle, and so on, until that of the *n*-th particle is finished. Next, we calculate the scattering coefficient error of the same particle between the neighboring steps and iterate the calculation until the error satisfying the requirement. Last, the internal field coefficient and heat generation of each particle are calculated. To valid of the algorithm, the results of initial simulation are compared with the experimental results (Reinhard et al., 2005) (see Fig. 4a and b). It can be seen the results are in good agreement. The small deviation of peak values is due to inaccuracy of the dielectric constant of media.

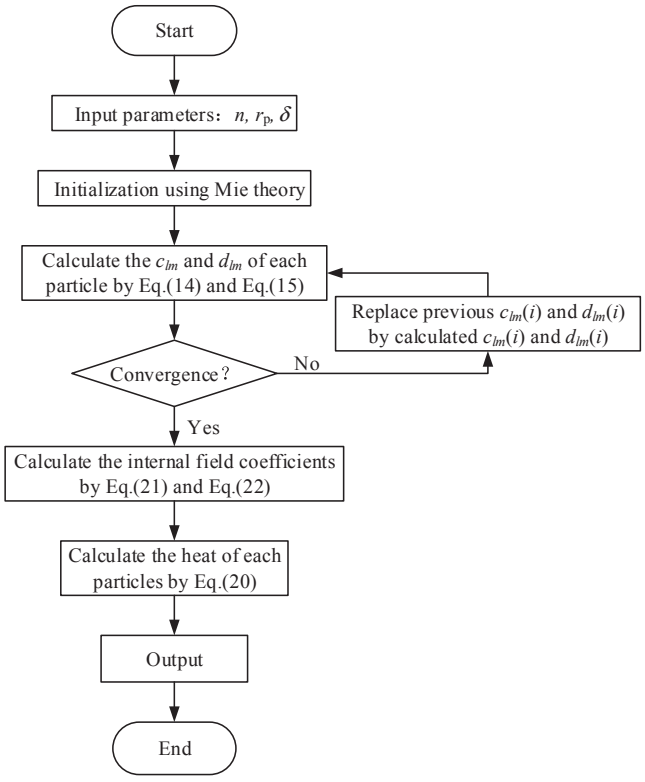

Fig. 3. Program chart.

To verify the robust of calculation, the calculation results are compared with the simulation results (Encina and Coronado, 2010) (Fig. 4c and d). The curves are completely agreement despite of the peak value is larger than that of the literature. The analysis shows that our results are more reliable since the electric field vibrates along the line linking the particle centers. The scattering fields is enhanced by the particle interaction and the extinction effect (Tabor et al., 2009). The peak value of coefficient is smaller than that of a single particle. Therefore, the calculation results have good accuracy and credibility. In addition, we calculate the absorption coefficient of a single gold nanoparticle in water at a wavelength of 280–2300 nm. Compared with the AM1.5 solar spectrum, we found that the solar energy is concentrated in visible light as well as the near-infrared region and the absorbance of gold nanoparticles above wavelengths of 900 nm is close to zero. So the wavelength range calculated here is selected from 280 to 900 nm.

3. Results and discussion

3.1. Particle pair

The optical and heating properties of a particle pair are first studied. The resulting absorption spectrum is consistent with the previous results (Fig. 5). In horizontal vibration mode, the resonance peaks show a blue shift and the intensity decreases with increasing of the inter-particle spacing (see Fig. 5a), illustrating the horizontal vibration mode enhanced the resonance. While in vertical vibration mode, the resonance peak presents a red shift and the intensity increases and approaches to that of a single-particle case (see Fig. 5b). This discloses that the horizontal resonance is suppressed by the vertical resonance mode. However, the resonance enhancement amplitude as well as the peak offset in horizontal vibration mode is larger than that of the vertical vibration mode, e.g. the horizontal vibration mode is shifted by 10 nm, while the vertical vibration mode is shifted by 3 nm.

Fig. 5c shows the heat production of a single particle from the pair at various spacings. The black curves and blue curves present the heat generation in the vertical vibration mode and horizontal vibration mode, respectively. It can be seen that the curve tendency is the same as that of the resonant peak shift (Sonnichsen et al., 2005). With the increase of spacing, the heat production of nanoparticle increases at the vertical vibration mode and decreases at the horizontal vibration mode, exhibiting an exponential relationship. To the best of our knowledge, this is the first time report on this phenomenon. According to the exponential-decay law, the interparticle distance can be evaluated from the heat generation. The red curve in Fig. 5c shows the total heat generation from the both vibrations. The total heat production of individual particles has the same decay law with the particle in horizontal vibration modes. This is because the heat generation of the horizontal vibration mode dominates in the overall heating. The following analysis thus focus on analyzing the distribution of electric field in horizontal vibration mode.

Fig. 5d shows the distribution of electric field around the particles in horizontal vibration mode (I, III, V) and the vertical vibration mode (II, IV, VI) (color scale uses logarithmic coordinates). Inset I indicates that the electric field in particle gaps is enhanced by plasmon interaction (Rechberger et al., 2003), while that of in the inset II is not enhanced. As the distance δ increases, the electric field enhancement across the nanoparticle gaps becomes smaller and smaller, and the electric field is almost decoupled at a gap of ~22.5 nm.

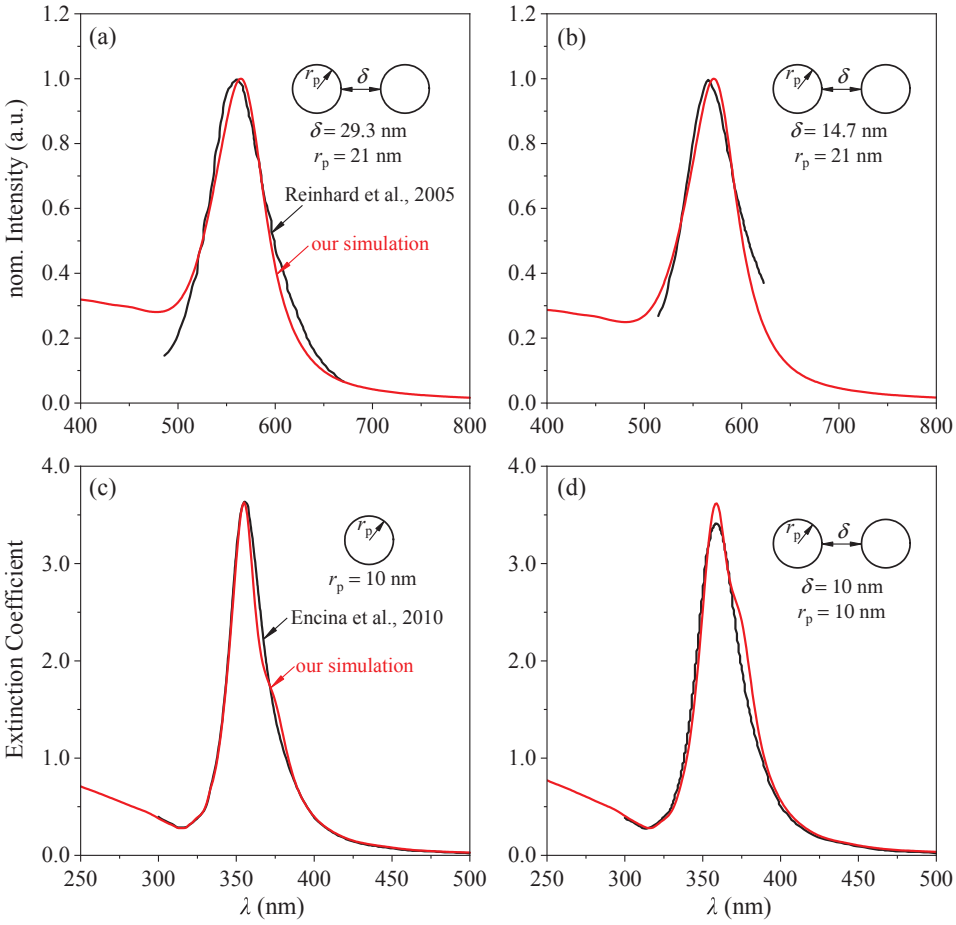

Fig. 4. Validation of the simulation with the reported results in literature. (a and b) show the experimental results of absorption spectra of the two interacting gold nanoparticles, and the dielectric constant of surrounding medium (DNA solution) was 2.56. (c) and (d) are the simulation results of absorption spectra of the silver nanoparticle in water, respectively.

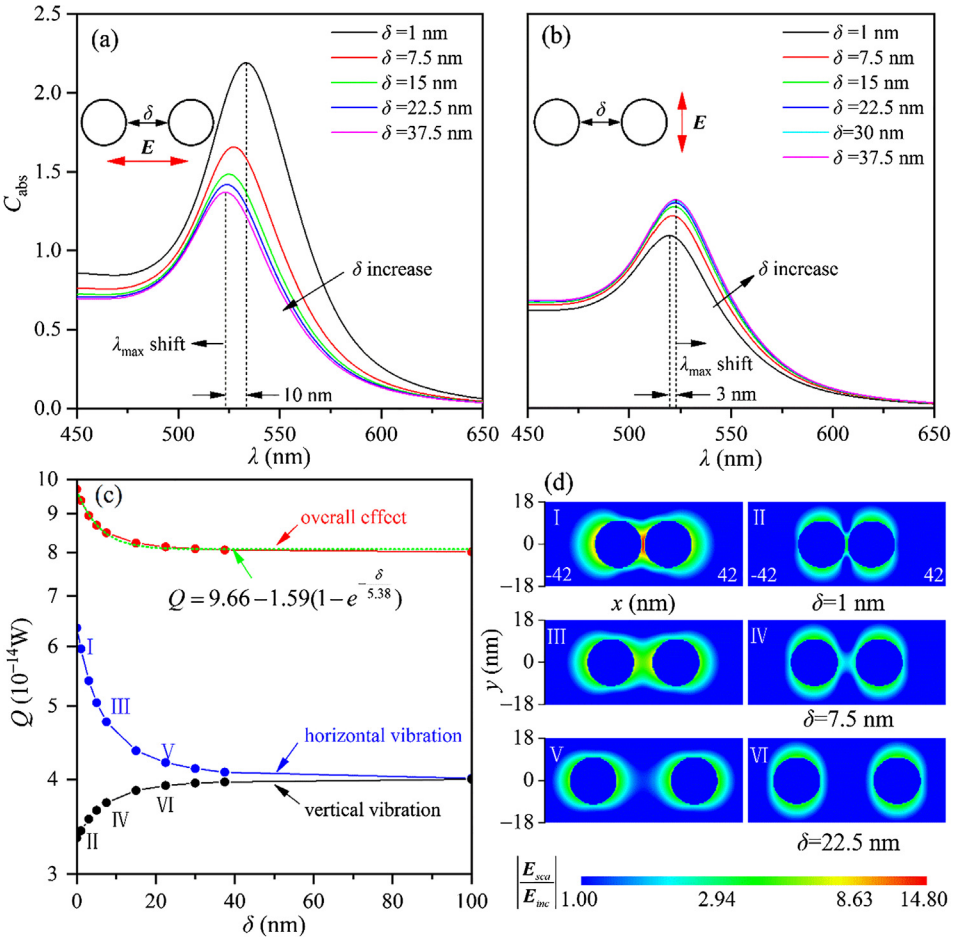

Fig. 5. The calculation results of a nanoparticle pair. (a) Blue-shifted of plasmon peak with increasing spacing δ and the electric field vibration paralleling to the chain axis. (b) Red-shifted of plasmon peak with increasing spacing and the electric field vibrating vertically to the chain axis. (c) Heat generation of one particle in horizontal vibration mode and vertical vibration mode at different interparticle gaps. The coexistence of two modes above is considered in overall effect. (d) The electric field distribution in surrounding medium with different interparticle gaps. (The color coordinates of scattered electric field in medium environment are logarithmic coordinates.) (For interpretation of the references to colour in this figure legend, the reader is referred to the web version of this article.)

3.2. Exponential decay of heat generation

The parallel polarization is examined here to illustrate the law of heat production in particle pair. Assume that the solar spectral irradiance at the particle resonance peak is the same within the calculation domain. The polarization mode of gold nanoparticles is a dipole. According to the dipole oscillation theory of electromagnetic field (Maier, 2007), the sum of electric field including the dipole near-field, middle and far-field regions can be expressed

$$\boldsymbol{E}\mathrm{sca} = \frac{1}{4\pi\varepsilon_0\varepsilon_2}\left\{\boldsymbol{k}^2(\boldsymbol{n}\times\boldsymbol{p})\times\boldsymbol{n}\frac{e^{i\boldsymbol{kr}}}{r} + [3\boldsymbol{n}(\boldsymbol{n}\cdot\boldsymbol{p})-\boldsymbol{p}]\left(\frac{1}{r^3}-\frac{i\boldsymbol{k}}{r^2}\right)e^{i\boldsymbol{kr}}\right\} \tag{23}$$

where, $\boldsymbol{n}$ is the unit vector in the direction of an any point K, $\boldsymbol{p}$ is the polarization intensity of the nanoparticle, and r is the distance between an any point K in space and the dipole. When the parallel polarized occurs, $\boldsymbol{n}$ and $\boldsymbol{p}$ are in the same direction. The scattered electric field strength of dipole can be abbreviated as

$$\boldsymbol{E}\mathrm{sca} = \frac{2\boldsymbol{p}}{4\pi\varepsilon_0\varepsilon_2}\frac{1}{r^3}(1-ikr)e^{ikr} \tag{24}$$

When the two particles are close to each other, they influence the charge distribution on their surface, which in turn affects the nanoparticle polarization. Therefore, the incident field of one of the particles is the superposition of the intensity of external electric field $\boldsymbol{E}_0$ with that of another particle dipole scatter electric field $\boldsymbol{E}_{\mathrm{sca}}$.

$$\boldsymbol{E}_{\mathrm{inc}} = \boldsymbol{E}_0 + \frac{2\boldsymbol{p}}{4\pi\varepsilon_0\varepsilon_2}\frac{1}{r^3}(1-ikr)e^{ikr} \tag{25}$$

As we known that $\boldsymbol{p} = \alpha\varepsilon_0\varepsilon_2\boldsymbol{E}_{\mathrm{inc}}$. When the distance between the centers of two nanoparticles is L, $\beta = (1-\mathrm{i}kL)e^{\mathrm{i}kL}$, $kL \ll 1$ and $\beta \approx 1$ in the near-field region, we can thus derive

$$\boldsymbol{E}_{\mathrm{inc}} = \frac{\boldsymbol{E}_0}{1-\frac{\alpha}{2\pi L^3}} \tag{26}$$

where the polarizability is $\alpha = \frac{1}{2}\pi D_p^3\frac{\varepsilon_1(\lambda)-\varepsilon_2}{\varepsilon_1(\lambda)+2\varepsilon_2}$, D_{p} is the nanoparticle diameter. When the nanoparticle spacing changes, the resonant wavelength as well as $\varepsilon_1(\lambda)$ also changes. When the electric field intensity of the incident light is $\boldsymbol{E}_{\mathrm{inc}}$, the electric field strength inside the nanoparticle is described as:

$$\boldsymbol{E}_{\mathrm{in}} = -\frac{3\varepsilon_2}{2\varepsilon_2+\varepsilon_1(\lambda)}\boldsymbol{E}_{\mathrm{inc}} \tag{27}$$

The heat power of nanoparticle is calculated as:

$$P(\lambda) = \frac{1}{2}\varepsilon_0\omega\,\mathrm{Im}[\varepsilon_1(\lambda)]\,|\boldsymbol{E}_{\mathrm{in}}|^2 \tag{28}$$

$\varepsilon_1(\lambda)$ can be expressed as $\varepsilon_{\mathrm{Re}}(\lambda) + \varepsilon_{\mathrm{Im}}(\lambda)\mathrm{i}$. Then we discuss the variation of the internal electric field of nanoparticle with the spacing and the wavelength.

$$\boldsymbol{E}_{\mathrm{in}} = -\frac{3\varepsilon_2}{2\varepsilon_2+\varepsilon_1(\lambda)}\boldsymbol{E}_{\mathrm{inc}} = \frac{-12\varepsilon_2\boldsymbol{E}_0}{(4\varepsilon_1(\lambda)+8\varepsilon_2)-(\frac{D_p}{L})^3(\varepsilon_1(\lambda)-\varepsilon_2)} \tag{29}$$

The above formula is simplified in respect of Buddha's power condition, assuming it satisfies at a certain wavelength of λ_r

$$(4\varepsilon_{\mathrm{Re}}(\lambda_r)+8\varepsilon_2)-(\frac{D_p}{L})^3(\varepsilon_{\mathrm{Re}}(\lambda_r)-\varepsilon_2) = 0 \tag{30}$$

that is

$$\varepsilon_{\mathrm{Re}}(\lambda_r) = \frac{(\frac{D_p}{L})^3 + 8}{(\frac{D_p}{L})^3 - 4}\varepsilon_2 \tag{31}$$

then $\boldsymbol{E}_{\mathrm{in}}$ gets the maximum value

$$\boldsymbol{E}_{\mathrm{in,max}} = \frac{12\varepsilon_2 \boldsymbol{E}_0 \mathrm{i}}{\left[4 - \left(\frac{D_p}{L}\right)^3\right]\varepsilon_{\mathrm{Im}}(\lambda_r)} \tag{32}$$

Substituting this into Eq. (28), we obtain

$$P_{\max}(\lambda_r) = \frac{1}{2}\varepsilon_0 \omega \left| \frac{12\varepsilon_2 \boldsymbol{E}_0}{4 - \left(\frac{D_p}{L}\right)^3} \right|^2 \frac{1}{|\varepsilon_{\mathrm{Im}}(\lambda_r)|} \tag{33}$$

The real part and the imaginary part of the dielectric constant of gold in the wavelength band of 500–600 nm are approximately linear with the wavelength. The relationship between the real part of the dielectric constant and the wavelength is $\varepsilon_{\mathrm{Re}}(\lambda) = 29.8896 - 0.0617\lambda$, and the relationship between the imaginary part and the wavelength is $\varepsilon_{\mathrm{Im}}(\lambda) = 11.7388 - 0.0174\lambda$. From the slope, it is seen that the dielectric constant varies little with the wavelength. Since $\varepsilon_{\mathrm{Im}}(\lambda)$ is not much change as the change of wavelength, the above formula is a function of the spacing $(\frac{D_p}{L})^3$, which can be approximated by an exponential relationship. The formula at other wavelength is similar to Eq. (33). Fig. 5c is the total heat generation of the sum value of the heat production of a particle over the whole wavelength. Thus, the heat generation exhibits exponential decay with the interparticle spacing which can be fitted as $Q = 9.66 - 1.59(1 - e^{-\frac{\delta}{5.38}})$. Substituting the linear fit of dielectric constant of into Eq. (29), and derivative it with the wavelength. We found that the value of function and the slope of each point on the curve decreased as the spacing decreases. It is demonstrated that the peak width of the curve decreases as the distance decreases.

3.3. Effect of particle number

For the plasmonic chains with a particle radius of 10 nm and an interparticle spacing of 1 nm, we calculate the heat production of chains by increasing the particle number from 2, 3, 5, 7 to 9. Fig. 6a shows the heat generation of each nanoparticle of the chains. It can be seen that as the number of particle increases, the heat generation in the intermediate nanoparticle increases and gradually approaches to a stable value. As the number of particles increases, the curve gradually present a flat shape at middle since the electromagnetic field has a certain active range. The center particles lies in a uniform electric field, resulting in strong heat production without the influence of the "boundary effect". This can also be distinguished from the difference in absorption coefficient of the particles located at the middle and the boundary (see Fig. 6b). Different curves represent the absorption difference between the center nanoparticle and its neighboring one in the plasmonic chains. As the number of nanoparticles increases, the absorption difference decreases with a red-shift of the wavelength peak.

Fig. 6c describes this phenomenon from the perspective of electric field. It shows the diagram of electric field amplitude and the scattering field, respectively. The surface electric field of particle is induced by a dipole and the color scale bar is a linear coordinate. The color scale bar of surrounding scattering field is a logarithmic coordinate. From Fig. 6c, it can be seen that as the number of particle increases, the intensity of the scattered field around the intermediate nanoparticles gradually

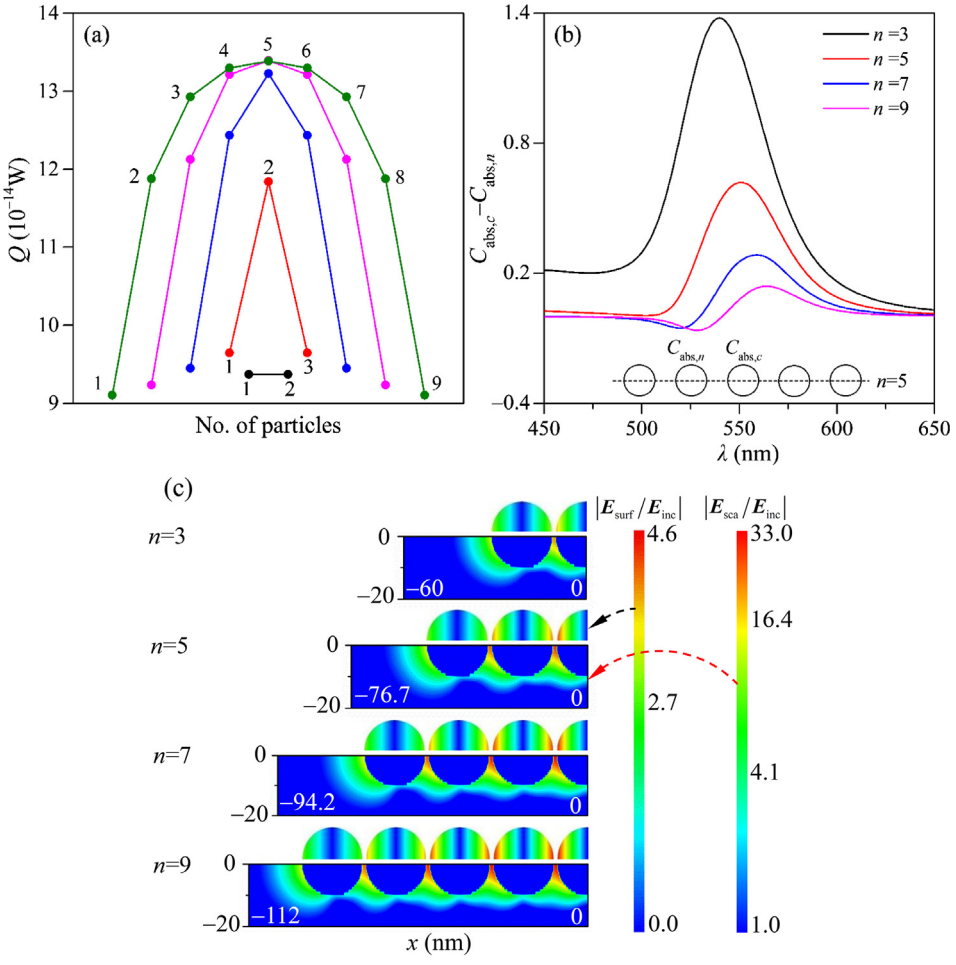

Fig. 6. Effect of particle number. The particle diameter is 20 nm and interparticle gap is 1 nm. (a) Heat generation of each particles. (b) The spectral line of $C_{abs,c}$-$C_{abs,n}$. $C_{abs,c}$ is the absorption coefficient of the center particle. $C_{abs,n}$ is the absorption coefficient of the neighbor particle of center particle. (c) Electric field distribution on the surface of particles and in the surrounding around particles. (The color coordinate system of the particles' surface electric field is the linear coordinate. The color coordinates of scattered electric field in medium environment are logarithmic coordinates.) (For interpretation of the references to colour in this figure legend, the reader is referred to the web version of this article.)

becomes strong without the "boundary effect". A conclusion can be drawn from the Mie scattering theory that the internal field of the particle is a response of the surrounding scattered field. Therefore, the enhanced field strength on the particle surface can be evaluated from the scattering field around the particle. According to Eq. (28), the heat production of particles is related to its electric field intensity. Since the number of particle increases, the intermediate nanoparticles are in an equivalent uniform electric field environment, resulting in the curve shape in Fig. 6a.

3.4. Effect of interparticle spacing

As the nanoparticle radius is 10 nm and the number of nanoparticles is seven, the heat production of particle chain with interparticle spacing of 1, 7.5, 15, 22.5, 30 and 37.5 nm are calculated (Fig. 7). With the increase of particle spacing, the heat production in intermediate nanoparticle decreases and approaches to the heat generation of an individual particle (red dashed line). This is because the particle interaction has a certain active range on its electromagnetic field. The intermediate particles in a same uniform electric field lead to their heat production to be consistent. When the particle spacing is 1 nm, and the heat production of the intermediate particle is 1.65 times larger than that of a single particle. This indicates that the spacing reducing between particles can greatly enhance the heat production of nanoparticle and improve the photothermal conversion efficiency. Fig. 7b shows the absorption coefficient of the fourth particle in horizontal vibration mode as the change of interparticle spacing. With the decrease of distance, the resonance intensity increases sharply with a red shift of the peaks. The heat output of intermediate particle also shows an exponential decay with the increasing of spacing. Fig. 7c shows the electric field and the scattered field intensity around the particles. The electric field on the surface of particles is produced by the dipole and the color scale bar is linear. The color scale bar of the scattered field is logarithmic coordinate. As the particle spacing increases, the enhanced amplitude of the scattering field around the particles tends to be consistent and decreases. The electric field on the particle surface also has the similar trend.

3.5. Effect of particle size

The particle size determines the particle absorption coefficient. When the nanoparticle size is small, the absorption coefficient is approximately to the extinction coefficient. The heat production of a particle depends on its size. For comparison, the heat production per unit volume is calculated for each nanoparticles. For the case of interparticle gap of 7.5 nm and the number of nanoparticle are seven. Fig. 8 shows the heat generation of each nanoparticle at different particle-radius under solar illumination. As the increases of particle radius, the middle of curve upwards and the heat production per unit volume also increases. This is because the enhanced scattering of large particle gives rise to the strong coupling effect of electromagnetic fields, which extends the "boundary effect" of electromagnetic fields. In contrast, the

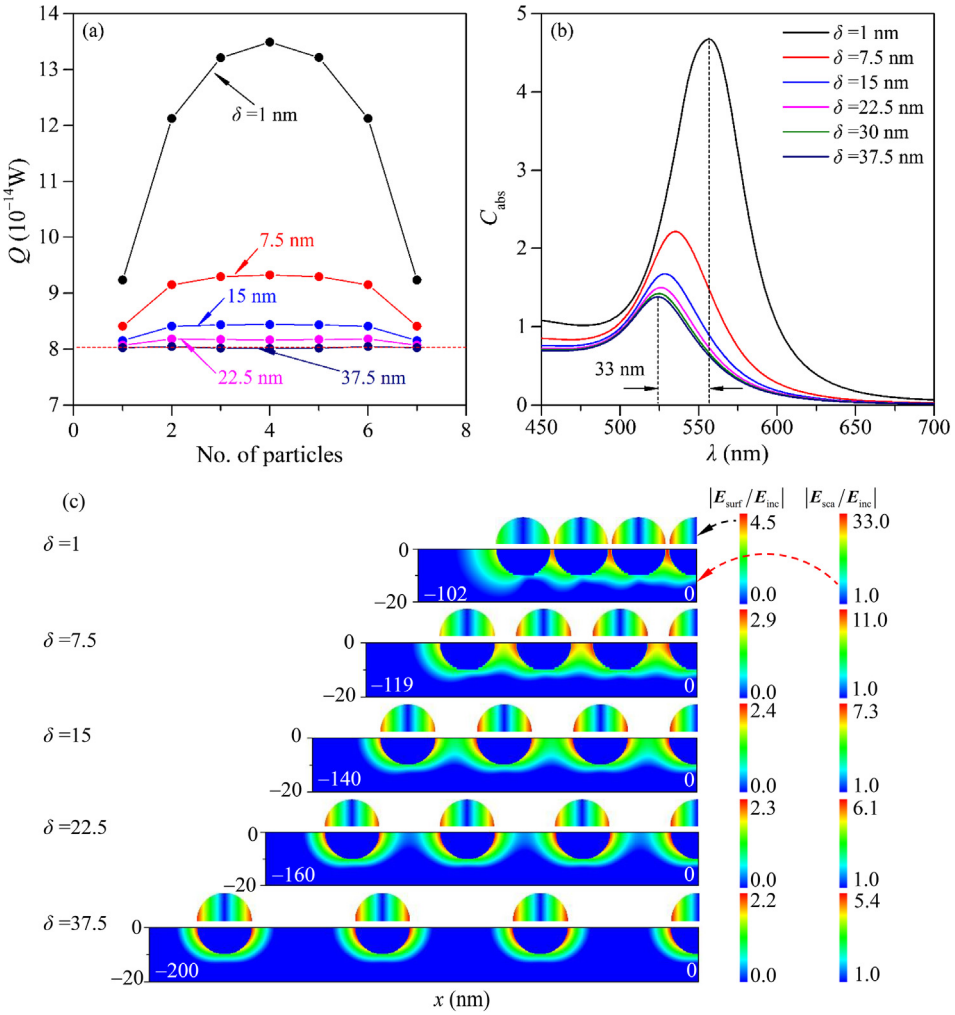

Fig. 7. Effect of inter-particle spacing. The particle diameter is 20 nm and the number are 7. (a) Heat generation of each particles. (b) Spectral line of the absorption coefficient of the center particle. (c) Electric field distribution on the particle surface and in the surrounding around the particles.

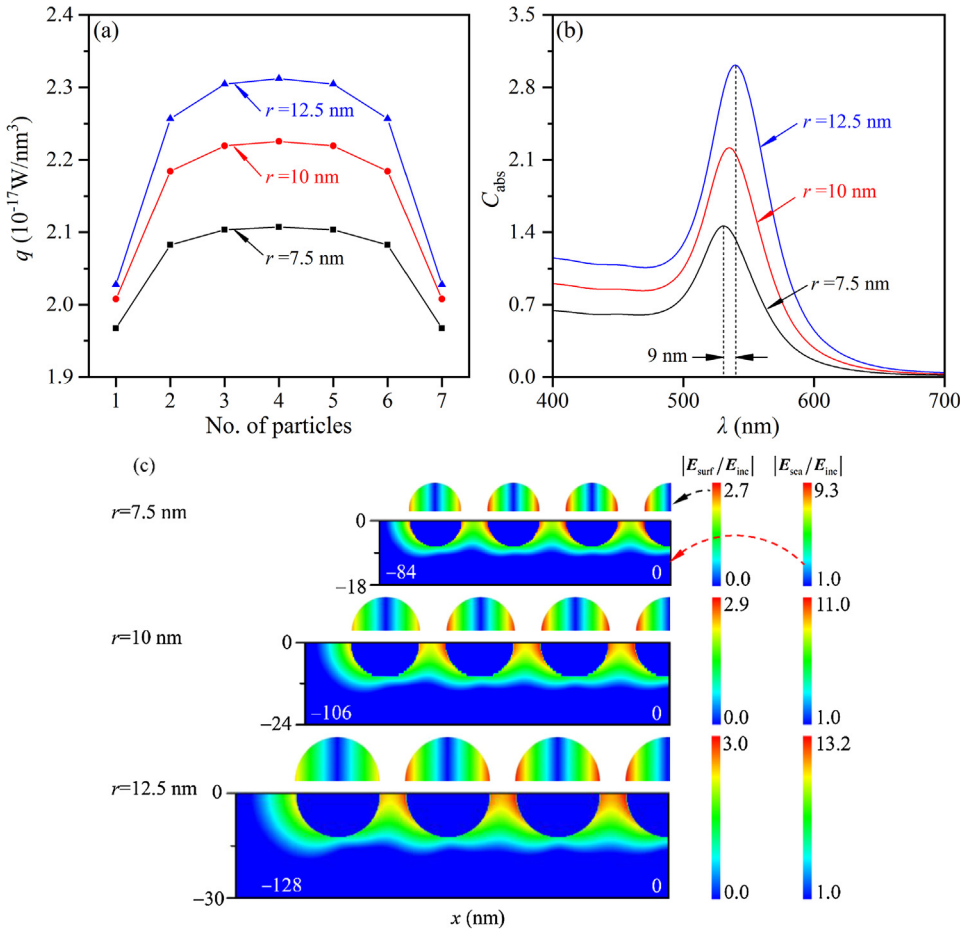

Fig. 8. Effect of particle radius. The interparticle gap is 7.5 nm and the number are 7. (a) Heat generation of each particles. (b) Spectral line of the absorption coefficient of the center particle. (c) Electric field distribution on the particle surface and in the surrounding medium.

curve of nanoparticle with a small size is flat in the middle. This indicates that the heat production of intermediate nanoparticles are approaching to a stable value without disturbance of the boundary effect.

4. Conclusions

We introduce a numerical technique to study the plasmon heating in one-dimensional plasmon chains of spherical nanoparticles that subject to external illumination. Electromagnetic and thermal calculations are performed based upon a General Mie Theory and Poynting vector method, respectively. The effect of particle number, interparticle gap and particle size on the plasmon heating are systematically analyzed to illustrate the heat distribution of plasmon chains. It was found that as the number of particle increased, the heat production of intermediate nanoparticle was increased with a tendency to approach a stable value. Regardless of the electron tunneling effect, the heat production of particle gradually increased with decreasing of the inter-particle spacing. This is because that the particles absorb more energy due to the enhanced electromagnetic-field coupling, which is eventually translated into heat energy. As the particle radius increases, it effectively increases the cross-section of absorption as well as the active range of electromagnetic radiation, and thus more light energy can be absorbed and converted into heat. Importantly, when the particle spacing is 1 nm, the particle numbers are seven and the radius is 10 nm, the heat production of intermediate particle is 1.65 times than that of a single particle. The heat production of the particles exponentially decays as reducing of the spacing between particles. This is consistent to the reported results that used to evaluate the distance between particles (Jain et al., 2007; Sonnichsen et al., 2005). Our work allows predicting heat generation of any individual particle in the plasmon chains by photothermal absorption. This opens a new route toward nanoscale control of thermal activation, local heating and heat dissipation, with potential applications to renewable energy, sensing and drug delivery.

Conflict of interest

The authors declare no competing financial interest.

Acknowledgements

The authors acknowledge the support from the Nature Science Foundation of China (51576002 and 51436004) and the Fundamental Research Funds for the Central Universities (2018QN020).

References

Baffou, G., Quidant, R., de Abajo, F.J.G., 2010. Nanoscale control of optical heating in complex plasmonic systems. ACS Nano 4 (2), 709–716.
Barrow, S.J., Funston, A.M., Gomez, D.E., Davis, T.J., Mulvaney, P., 2011. Surface plasmon resonances in strongly coupled gold nanosphere chains from monomer to hexamer. Nano Lett. 11 (10), 4180–4187.
Barrow, S.J., Rossouw, D., Funston, A.M., Botton, G.A., Mulvaney, P., 2014. Mapping bright and dark modes in gold nanoparticle chains using electron energy loss spectroscopy. Nano Lett. 14 (7), 3799–3808.
Chen, M., He, Y., Wang, X., Hu, Y., 2018. Numerically investigating the optical properties of plasmonic metallic nanoparticles for effective solar absorption and heating. Sol. Energy 161, 17–24.
Citrin, D.S., 2004. Coherent excitation transport in metal-nanoparticle chains. Nano Lett. 4 (9), 1561–1565.
Cognet, L., Tardin, C., Boyer, D., Choquet, D., Tamarat, P., Lounis, B., 2003. Single metallic nanoparticle imaging for protein detection in cells. Proc. Natl. Acad. Sci. 100

(20), 11350–11355.
Cruzan, O., 1962. Translational addition theorems for spherical vector wave functions. Q. Appl. Math. 33–40.
Ding, T., Valev, V.K., Salmon, A.R., Forman, C.J., Smoukov, S.K., Scherman, O.A., Frenkel, D., Baumberg, J.J., 2016. Light-induced actuating nanotransducers. Proc. Natl. Acad. Sci. 113 (20), 5503–5507.
Downing, C.A., Mariani, E., Weick, G., 2018. Retardation effects on the dispersion and propagation of plasmons in metallic nanoparticle chains. J. Phys. Condens. Matter: Inst. Phys. J. 30 (2) 025301.
Encina, E.R., Coronado, E.A., 2010. Plasmon coupling in silver nanosphere pairs. J. Phys. Chem. C 114 (9), 3918–3923.
Esteban, R., Borisov, A.G., Nordlander, P., Aizpurua, J., 2012a. Bridging quantum and classical plasmonics with a quantum-corrected model. Nat. Commun. 3.
Esteban, R., Taylor, R.W., Baumberg, J.J., Aizpurua, J., 2012b. How chain plasmons govern the optical response in strongly interacting self-assembled metallic clusters of nanoparticles. Langmuir: ACS J. Surf. Colloids 28 (24), 8881–8890.
Fan, J.A., Wu, C., Bao, K., Bao, J., Bardhan, R., Halas, N.J., Manoharan, V.N., Nordlander, P., Shvets, G., Capasso, F., 2010. Self-assembled plasmonic nanoparticle clusters. Science 328 (5982), 1135–1138.
G173, 2007. Standard Tables for Reference Solar Spectral Irradiances: Direct Normal and Hemispherical on 37° Tilted Surface. ASTM International G 173-03.
Gérardy, J.M., Ausloos, M., 1982. Absorption spectrum of clusters of spheres from the general solution of Maxwell's equations. II. Optical properties of aggregated metal spheres. Phys. Rev. B 25 (6), 4204–4229.
Ghosh, S.K., Pal, T., 2007. Interparticle coupling effect on the surface plasmon resonance of gold nanoparticles: from theory to applications. Chem. Rev. 107 (11), 4797–4862.
Govorov, A.O., Zhang, W., Skeini, T., Richardson, H., Lee, J., Kotov, N.A., 2006. Gold nanoparticle ensembles as heaters and actuators: melting and collective plasmon resonances. Nanoscale Res. Lett. 1 (1), 84–90.
Halas, N.J., Lal, S., Chang, W.S., Link, S., Nordlander, P., 2011. Plasmons in strongly coupled metallic nanostructures. Chem. Rev. 111 (6), 3913–3961.
Haynes, C.L., McFarland, A.D., Zhao, L., Van Duyne, R.P., Schatz, G.C., Gunnarsson, L., Prikulis, J., Kasemo, B., Käll, M., 2003. Nanoparticle optics: the importance of radiative dipole coupling in two-dimensional nanoparticle arrays. J. Phys. Chem. B 107 (30), 7337–7342.
Hentschel, M., Saliba, M., Vogelgesang, R., Giessen, H., Alivisatos, A.P., Liu, N., 2010. Transition from isolated to collective modes in plasmonic oligomers. Nano Lett. 10 (7), 2721–2726.
Herrmann, L.O., Valev, V.K., Tserkezis, C., Barnard, J.S., Kasera, S., Scherman, O.A., Aizpurua, J., Baumberg, J.J., 2014. Threading plasmonic nanoparticle strings with light. Nat. Commun. 5, 4568.
Hicks, E.M., Zou, S., Schatz, G.C., Spears, K.G., Van Duyne, R.P., Gunnarsson, L., Rindzevicius, T., Kasemo, B., Käll, M., 2005. Controlling plasmon line shapes through diffractive coupling in linear arrays of cylindrical nanoparticles fabricated by electron beam lithography. Nano Lett. 5 (6), 1065–1070.
Jackson, J.D., 2001. Classical Electrodynamics. John Wiley & Sons Inc.
Jain, P.K., Huang, W., El-Sayed, M.A., 2007. On the universal scaling behavior of the distance decay of plasmon coupling in metal nanoparticle pairs: a plasmon ruler equation. Nano Lett. 7 (7), 2080–2088.
Johnson, P.B., Christy, R.W., 1972. Optical constants of the noble metals. Phys. Rev. B 6 (12), 4370–4379.
Jung, H., Cha, H., Lee, D., Yoon, S., 2015. Bridging the nanogap with light: continuous tuning of plasmon coupling between gold nanoparticles. ACS Nano 9 (12), 12292–12300.
Kuzyk, A., Schreiber, R., Fan, Z., Pardatscher, G., Roller, E.-M., Högele, A., Simmel, F.C., Govorov, A.O., Liedl, T., 2012. DNA-based self-assembly of chiral plasmonic nanostructures with tailored optical response. Nature 483 (7389), 311–314.
Lal, S., Link, S., Halas, N.J., 2007. Nano-optics from sensing to waveguiding. Nat. Photonics 1 (11), 641–648.
Lee, B.J., Park, K., Walsh, T., Xu, L., 2012. Radiative heat transfer analysis in plasmonic nanofluids for direct solar thermal absorption. J. Sol. Energy Eng. 134 (2) 021009.
Lin, S., Li, M., Dujardin, E., Girard, C., Mann, S., 2005. One-dimensional plasmon coupling by facile self-assembly of gold nanoparticles into branched chain networks. Adv. Mater. 17 (21), 2553–2559.
Mackowski, D.W., 1991. Analysis of radiative scattering for multiple sphere configurations. Proc. R. Soc. A: Math. Phys. Eng. Sci. 433 (1889), 599–614.
Maier, S.A., 2007. Plasmonics: Fundamentals and Applications. Springer US.
Maier, S.A., Kik, P.G., Atwater, H.A., Meltzer, S., Harel, E., Koel, B.E., Requicha, A.A.G., 2003. Local detection of electromagnetic energy transport below the diffraction limit in metal nanoparticle plasmon waveguides. Nat. Mater. 2 (4), 229–232.
Manoharan, V.N., Elsesser, M.T., Pine, D.J., 2003. Dense packing and symmetry in small clusters of microspheres. Science 301 (5632), 483–487.
Mie, G., 1908. Beitrage Zur Optik Trber Medien, speziell kolloidaler Metallösungen. Annalen der physik 330 (3), 377–445.
Montelongo, Y., Sikdar, D., Ma, Y., McIntosh, A.J.S., Velleman, L., Kucernak, Anthony R., Edel, J.B., Kornyshev, A.A., 2017. Electrotunable nanoplasmonic liquid mirror. Nat. Mater. 16 (11), 1127–1135.
Mortensen, N.A., Raza, S., Wubs, M., Søndergaard, T., Bozhevolnyi, S.I., 2014. A generalized non-local optical response theory for plasmonic nanostructures. Nat. Commun. 5.
Nie, Z., Petukhova, A., Kumacheva, E., 2010. Properties and emerging applications of self-assembled structures made from inorganic nanoparticles. Nat. Nanotechnol. 5 (1), 15–25.
Nordlander, P., Oubre, C., Prodan, E., Li, K., Stockman, M.I., 2004. Plasmon hybridization in nanoparticle dimers. Nano Lett. 4 (5), 899–903.
Qian, Z., Ginger, D.S., 2017. Reversibly reconfigurable colloidal plasmonic nanomaterials. J. Am. Chem. Soc. 139 (15), 5266–5276.
Rechberger, W., Hohenau, A., Leitner, A., Krenn, J.R., Lamprecht, B., Aussenegg, F.R., 2003. Optical properties of two interacting gold nanoparticles. Opt. Commun. 220 (1–3), 137–141.
Reinhard, B.M., Siu, M., Agarwal, H., Alivisatos, A.P., Liphardt, J., 2005. Calibration of dynamic molecular rulers based on plasmon coupling between gold nanoparticles. Nano Lett. 5 (11), 2246–2252.
Richardson, H.H., Hickman, Z.N., Govorov, A.O., Thomas, A.C., Zhang, W., Kordesch, M.E., 2006. Thermooptical properties of gold nanoparticles embedded in ice: characterization of heat generation and melting. Nano Lett. 6 (4), 783–788.
Ross, M.B., Mirkin, C.A., Schatz, G.C., 2016. Optical properties of one-, two-, and three-dimensional arrays of plasmonic nanostructures. J. Phys. Chem. C 120 (2), 816–830.
Sanchot, A., Baffou, G., Marty, R., Arbouet, A., Quidant, R., Girard, C., Dujardin, E., 2012. Plasmonic nanoparticle networks for light and heat concentration. ACS Nano 6 (4), 3434–3440.
Scanlon, M.D., Smirnov, E., Stockmann, T.J., Peljo, P., 2018. Gold nanofilms at liquid-liquid interfaces: an emerging platform for redox electrocatalysis, nanoplasmonic sensors, and electrovariable optics. Chem. Rev. 118 (7), 3722–3751.
Skirtach, A.G., Dejugnat, C., Braun, D., Susha, A.S., Rogach, A.L., Parak, W.J., Möhwald, H., Sukhorukov, G.B., 2005. The role of metal nanoparticles in remote release of encapsulated materials. Nano Lett. 5 (7), 1371–1377.
Sonnichsen, C., Reinhard, B.M., Liphardt, J., Alivisatos, A.P., 2005. A molecular ruler based on plasmon coupling of single gold and silver nanoparticles. Nat. Biotechnol. 23 (6), 741–745.
Stein, S., 1961. Addition theorems for spherical wave functions. Q. Appl. Math. 19 (1), 15–24.
Tabor, C., Murali, R., Mahmoud, M., El-Sayed, M.A., 2009. On the use of plasmonic nanoparticle pairs as a plasmon ruler: the dependence of the near-field dipole plasmon coupling on nanoparticle size and shape. J. Phys. Chem. A 113 (10), 1946–1953.
Tan, S.J., Campolongo, M.J., Luo, D., Cheng, W., 2011. Building plasmonic nanostructures with DNA. Nat. Nanotechnol. 6 (5), 268–276.
Teulle, A., Bosman, M., Girard, C., Gurunatha, K.L., Li, M., Mann, S., Dujardin, E., 2015. Multimodal plasmonics in fused colloidal networks. Nat. Mater. 14 (1), 87–94.
Thomas, R., Swathi, R.S., 2016. Linear and polygonal assemblies of plasmonic nanoparticles: incident light polarization dictates hot spots. J. Phys. Chem. C 120 (33), 18733–18740.
Tian, L., Luan, J., Liu, K.-K., Jiang, Q., Tadepalli, S., Gupta, M.K., Naik, R.R., Singamaneni, S., 2015. Plasmonic biofoam: a versatile optically active material. Nano Lett. 16 (1), 609–616.
Tserkezis, C., Herrmann, L.O., Valev, V.K., Baumberg, J.J., Aizpurua, J., 2014. Optical response of threaded chain plasmons: from capacitive chains to continuous nanorods. Opt. Express 22 (20), 23851–23860.
Wang, H., Chen, L., Shen, X., Zhu, L., He, J., Chen, H., 2012. Unconventional chain-growth mode in the assembly of colloidal gold nanoparticles. Angew. Chem. Int. Ed. Engl. 51 (32), 8021–8025.
Wang, X., He, Y., Liu, X., Shi, L., Zhu, J., 2017. Investigation of photothermal heating enabled by plasmonic nanofluids for direct solar steam generation. Sol. Energy 157, 35–46.
Zhang, H., Wang, D., 2008. Controlling the growth of charged-nanoparticle chains through interparticle electrostatic repulsion. Angew. Chem. 120 (21), 4048–4051.
Zhu, W., Crozier, K.B., 2014. Quantum mechanical limit to plasmonic enhancement as observed by surface-enhanced Raman scattering. Nat. Commun. 5, 5228.
Zou, S., Schatz, G.C., 2006. Theoretical studies of plasmon resonances in one-dimensional nanoparticle chains: narrow lineshapes with tunable widths. Nanotechnology 17 (11), 2813–2820.
Zuloaga, J., Prodan, E., Nordlander, P., 2009. Quantum description of the plasmon resonances of a nanoparticle dimer. Nano Lett. 9 (2), 887–891.